Materials Science & Engineering B 246 (2019) 89–95

Contents lists available at ScienceDirect

Materials Science & Engineering B

journal homepage: www.elsevier.com/locate/mseb

The effect of nanoparticle and mesoporous TiO_2 additions on the electronic characteristics of reduced graphene oxide nanocomposites with zinc oxide under UV irradiation

Sara Abbaspour[a], Amirabbas Nourbakhsh[b,*], Reza Ebrahimi[a], Hamid Ghayour[a], Kenneth J.D. Mackenzie[c,*]

[a] Advanced Materials Research Center, Department of Materials Engineering, Najafabad Branch, Islamic Azad University of Najafabad, PO Box 85141-43131, Najafabad, Isfahan, Iran
[b] Department of Materials Science and Engineering, Shahreza Branch, Islamic Azad University Shahreza Branch, Pasdaran Street, Shahreza 86145-311, Isfahan, Iran
[c] Macdiarmid Institute for Advanced Materials and Nanotechnology, Victoria University of Wellington, P.O. Box 600, Wellington, New Zealand

ARTICLE INFO

Keywords:
Electrical conductivity
Mesoporous TiO_2
Nanocomposites
Reduced graphene oxide-ZnO-TiO_2

ABSTRACT

Semiconducting nanocomposites were formed from layers of reduced graphene oxide (RGO) and ZnO and nanoparticle or mesoporous forms of TiO_2 by dip-coating on fluorine-doped tin oxide (FTO) substrates. The effect of nanoparticle or mesoporous TiO_2 on the electrical conductivity was compared. The crystalline phases and microstructures of the nanocomposites were investigated by XRD, DRS-UV, FTIR and FE-SEM, showing the layers to be homogeneous and of consistent thickness, with the TiO_2 in the anatase form. The bandgaps and electrical conductivities of the nanocomposites, determined by Tauc plots and electrochemical impedance spectroscopy (EIS), show that under UV irradiation, the nanocomposites containing nanoparticle TiO_2 have higher electrical conductivities than those containing mesoporous TiO_2. A mechanism is suggested involving the formation of nano-capacitors on the surface of the ZnO layer, the pores in the mesoporous TiO_2 acting as the dielectric and the conducting electrodes formed by UV irradiation of the TiO_2.

1. Introduction

Among various metal oxide semiconductors, TiO_2 [1] and ZnO [2,3] have been the most extensively studied due to their unique photocatalytic efficiency, low cost, nontoxicity, and high stability. However, the fast electron–hole pair recombination of TiO_2 and ZnO significantly limits their photocatalytic efficiency [4]. Xu et al. [5] have reported that graphene hybridized ZnO photocatalysts showed enhanced photocatalytic degradation of an organic dye, the degree of photocatalytic activity enhancement strongly depending on the coverage of the graphene on the surface of the ZnO nanoparticles [5]. This photocatalytic enhancement was attributed to the high migration efficiency of photoinduced electrons and the inhibition of charge carrier recombination due to the electronic interaction between the ZnO and the graphene [5]. ZnO/TiO_2 nanocomposites improved the electrical conductivity compared to ZnO and TiO_2 alone. One of the primary drawbacks of deposition of TiO_2 on ZnO nanorod systems is the poor quantum efficiency under visible light. The photocatalytic efficiency found for these photo catalytic systems is due to the fast recombination of electron–hole pairs [6,7]. The improved photocatalytic efficiency of a semiconductor hybridized with carbonaceous materials such as RGO has attracted attention in photocatalytic research and has been recently been a focus of the scientific community with regard to the beneficial role of carbonaceous materials hybridized with semiconductors to improve their photocatalytic efficiency [2,8,9]. Liu et al. [10] reported that ZnO composites with reduced graphene oxide (RGO) show improved photocatalytic performance compared with pure ZnO, ascribing this improvement to increased light absorption intensity and range and the inhibition of photoelectron–hole pair recombination in the ZnO by the introduction of RGO. The first report of electrospinning of TiO_2-ZnO-graphene composite into nanofibers for photovoltaic and biomedical applications was by Madhavan et al. [11]. The composite fibers were employed as photoanodes for DSSC applications, giving an efficiency of ~3.7%. Liu et al. [12] synthesized ZnO–TiO_2–reduced graphene oxide composites by a microwave-assisted reaction and reported that the resulting ZnO–TiO_2–RGO composites show better photocatalytic

* Corresponding authors.
E-mail addresses: anourbakhs@yahoo.com (A. Nourbakhsh), rezaebrahami@1aun.ac.ir (R. Ebrahimi), h-ghayour@iaun.ac.ir (H. Ghayour), kenneth.mackenzie@vuw.ac.nz (K.J.D. Mackenzie).

https://doi.org/10.1016/j.mseb.2019.06.003
Received 23 November 2017; Received in revised form 9 April 2019; Accepted 6 June 2019

activities than ZnO or ZnO-RGO composites alone. The photocatalytic performance of ZnO–TiO_2–RGO depends on the proportion of TiO_2 in the composites, the enhanced photocatalytic performance being ascribed to the increased light absorption intensity and the reduction of photoelectron–hole pair recombination in the ZnO with the introduction of the TiO_2. Tuz Johra et al. [13] confirmed that the photocatalytic activity of RGO–TiO_2–ZnO composites was superior to that of pure ZnO and TiO_2–ZnO, and showed that the presence of the TiO_2 nanoparticles in the RGO-ZnO nanocomposites reduced their total impedance, thus improving their electrical conductivity [13].

Although research during last decade showed that the nanocomposites RGO-ZnO-TiO_2 had better conductivity and photocatalytic efficiency, the role of different types of TiO_2 (e.g. mesoporous and nanoparticle forms) is not well understood. In this work we studied the effect of different types of TiO_2 (meso and nano) additions on the electrical conductivity of RGO-ZnO nanocomposites and discuss the mechanistic implications of these results.

2. Experimental

2.1. Synthesis of graphene oxide (GO) and reduced graphene oxide (RGO)

Graphene oxide nanoparticles were prepared from graphite by a modified Hummers method [14]. Prior to the synthesis, the graphite was leached by refluxing with boiling HCl for 45 min, then vacuum-filtered, washed five times with distilled water to remove the acid and dried under vacuum at 40 °C for 3 h. 1 g of the leached graphite nanoplatelets was then added to a solution of 23 mL concentrated H_2SO_4 and 0.5 g of KNO_3, followed by the slow addition of 3 g of $KMnO_4$, cooling the mixture in an ice bath at 0–5 °C. After standing at room temperature for 1 hr, 140 mL of deionized water and 10 mL of 10% H_2O_2 were added, and the resulting GO powder was ultrasonically separated from the solution, centrifuged and dried for 24 hr. in a vacuum oven. The impurity Mn ions were then removed by washing five times with HCl, then with water at 70 °C to remove the excess acid. The resulting powder was irradiated for 21 hr. at room temperature under two 15 W UV lamps, then reduced by calcining for 30 min. at 400 °C under argon.

2.2. Synthesis of ZnO

The ZnO powder were prepared by dissolving 14.75 g of Zn $(CH_3COO)_2{\cdot}2H_2O$ (99%, Sigma Aldrich) in 60 mL of ethanol and 5.2 g NaOH in 30 mL of ethanol. After ultrasonification, the two solutions were mixed and stirred at 60 °C for 72 h [15]. The white ZnO powder was then separated by centrifuging, washed with water and ethanol and dried under vacuum at 40 °C.

2.3. Synthesis of TiO_2 nanoparticles

5 mL of Ti $[OCH(CH_3)_2]_4$ was dissolved in 100 mL of isopropyl alcohol and stirred for 1 hr at room temperature. 400 mL of deionized water was then added rapidly and the resulting solution was aged for 3 hr before being dip-coated on to a fluorine-doped tin oxide (FTO) glass substrate (Sigma Aldrich, 15 Ohm) and calcined at 450 °C for 2 hr in argon atmosphere [16].

2.4. Synthesis of mesoporous TiO_2

1 g triblock copolymer (Pluronic P123, PEO22PPO72PEO22, Sigma Aldrich) was dissolved in 60 mL ethanol and 5.18 mL titanium isopropoxide (979, Sigma Aldrich) was added. This mixture was then added to 36 mL distilled water, maintaining the pH at 10 by the addition of ammonia solution. The resulting sol was aged at room temperature for 24 h, then coated on to FTO glass and heated under argon at 200 °C for 2 hr, then at 450 °C for 3 h to form the mesoporous structure [17].

Table 1
Description of the composite samples on FTO glass and their electrical measurement conditions.

Sample	Description	Electrical measurement conditions
1	RGO-ZnO-nanoparticle TiO_2	Visible radiation
2	RGO-ZnO-nanoparticle TiO_2	UV radiation
3	RGO-ZnO-mesoporous TiO_2	Visible radiation
4	RGO-ZnO-mesoporous TiO_2	UV radiation

2.5. Deposition of the various layers of the composite samples

The various layers of the composite samples (nanoparticle TiO_2, mesoporous TiO_2 and ZnO) were deposited by dip coating. A GO layer was deposited on an FTO glass substrate, followed by a layer of ZnO particles. A layer TiO_2, either of nanoparticle or mesoporous morphology, was then applied, and the assembly calcined at 400 °C in argon for 4 hr. The descriptions of the various samples and the conditions under which their electrical properties were measured are shown in Table 1.

2.6. Sample characterization

The crystalline components of the samples were identified by X-ray diffraction (Bruker Avance D8) using Cu radiation and a Ni filter. Fourier transform infrared spectroscopy was carried out using a Nicolet Impact 400D spectrometer, and diffuse reflectance-UV spectroscopy was carried out at 190–2700 nm using a JASCO spectrophotometer model V-670, Japan. The microstructures of the samples were studied by TEM (JEOL model JEM 2011) and SEM (LEO 435VP) and the surface morphology, structures, and compositions of the samples were characterized by field emission scanning electron microscopy (FE-SEM) and energy dispersive X-ray spectrometry (EDS) analyses (MIRA3TESCAN-XMU). The BET surface areas and pore volumes of the samples were determined at liquid nitrogen temperature, using a Gemini modele 2365 (Micromertic Company) apparatus Electrochemical impedance spectroscopy (EIS) was carried out using a Princeton Applied Research Model PARSTAT 2273, under UV light in a cell using an iodide/triiodide electrolyte (ELT-ACN-I-10ML, Sharifsolar Co), to compare the resistance of the samples containing the two forms of TiO_2. The BET surface areas and pore volumes of the TiO_2 samples were determined at liquid nitrogen temperature, using a Gemini model 2365 apparatus (Micromeritics Company).

3. Results and discussion

3.1. Characterization of the starting materials

3.1.1. Graphite, GO and RGO

Fig. 1a shows the XRD patterns of the graphite, GO and RGO. Graphite contains a strong sharp peak at $2\theta = 26^\circ$ arising from the (0 0 2) plane, and GO contains a reflection at $2\theta = 11^\circ$ from the (0 0 1) plane. The plane in graphene oxide reflects the presence of the oxygen-containing functional groups [18]. The lack of a graphite peak in the GO pattern indicates complete graphite oxidation and confirms the synthesis method [19]. Fig. 1a (III) shows the disappearance of the (0 0 1) GO reflection consistent with its reduction [20], which also produces a much-broadened (0 0 2) plane.

Fig. 1b shows the FTIR spectra in the range 450–4000 cm^{-1} of the leached graphite reactant, GO and RGO samples prepared under UV light. The spectra show the OH stretching band at 3420 cm^{-1}, the C=O carbonyl stretch at 1728 cm^{-1} and the C–O epoxide group stretch at 1225 and 1071 cm^{-1}. The peaks of the oxygen-containing functional

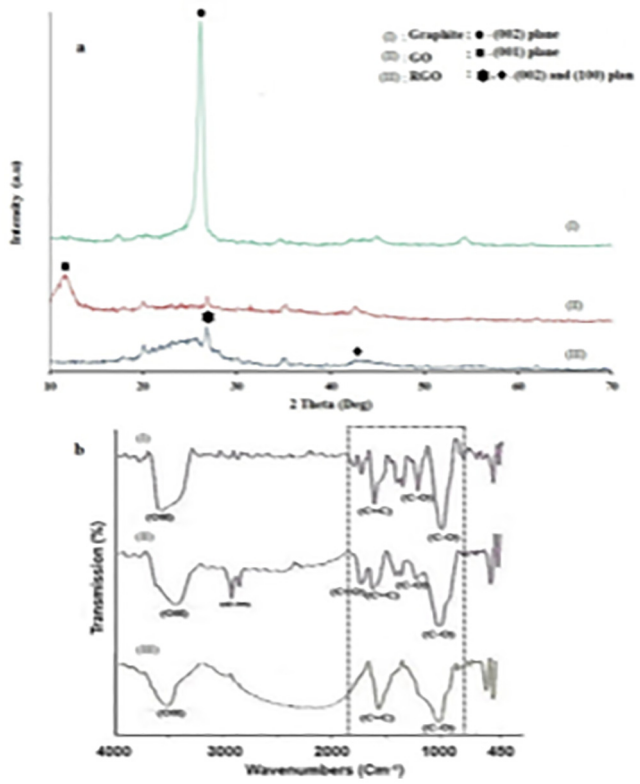

Fig. 1. a) XRD patterns, b) FTIR spectra of I) graphite, II) GO, III) RGO.

groups are almost completely removed in RGO (Fig. 1b (III)) and the intensity of the C=C band at 1620 $cm^{-1}$is increased, suggesting that the reduction of the graphene oxide is complete [21–23].

Typical SEM micrographs of the RGO nanoplatelets (Fig. 2) show both the layered and exfoliated structure aspects of the structure [24].

3.1.2. ZnO and nanoparticle and mesoporous TiO_2

The XRD patterns of the ZnO and TiO_2 starting materials (Fig. 3) indicate that both are crystalline, with the TiO_2 occurring solely in the anatase form. The presence of the (1 0 0) reflection in the low angle XRD pattern of the mesoporous TiO_2 (Fig. S1) is identical to that previously observed in mesoporous TiO_2 [17] and confirms the mesoporous structure of this phase.

The SEM micrographs of the ZnO particles and nanoparticle TiO_2 (Fig. 4a,b) show the particle size of the ZnO to be larger than that of the

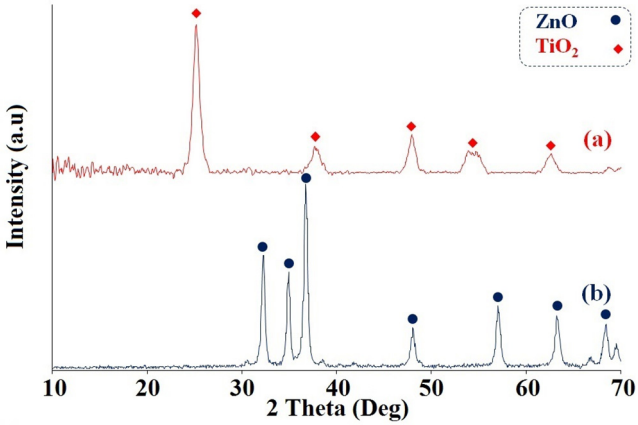

Fig 3. XRD patterns of a) TiO_2, b) ZnO.

TiO_2, and to contain a large proportion of rounded particles, possibly aggregates of smaller particles (Fig. 4a). By contrast, the morphology of the nanoparticle TiO_2 (Fig. 4b) consists of aggregates of much smaller particles. The TEM micrograph of the mesoporous TiO_2 (Fig. 4c) is as expected in this material [17] and shows this phase to possess a nano structure with a pore size in the range 5–10 nm [25].

The BET plot of the mesoporous TiO_2 and plot of ($\frac{dv_p}{dr_p}$) vs. r_p (nm) are shown in Fig. 5(a, b), where v_p and r_p are the pore volume and radius respectively. The data obtained from these plots (Table 2) were used to calculate the total pore surface and mean pore size ($\bar{d}$) by equations 1–3 [26].

$$S_t = \frac{V_m L_{av} A_m}{M_v} \quad (1)$$

$$V_m = \frac{1}{s + i} \quad (2)$$

$$\bar{d} = \frac{4\ V_p}{S_t} \quad (3)$$

where $L_{av} = 6.022 \times 10^{23}$ (Particle/mole), $A_m = 0.162\,nm^2$, $M_v = 22414\,cm^3$, S and I are the slope and intercept of the BET plot and v_p is pore volume.

These results showed a good correlation between the TEM microstructure and the BET measurements.

3.2. XRD characterization of the layer-structured nanocomposites

XRD analysis was carried out on two of the thin layered

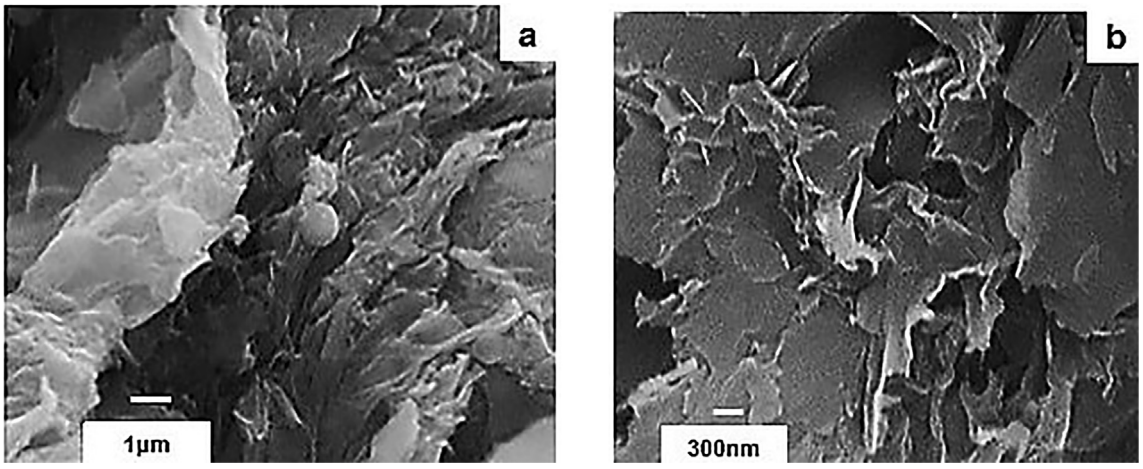

Fig. 2. SEM images of RGO. a) Magnification 8000x, b) magnification 15000x.

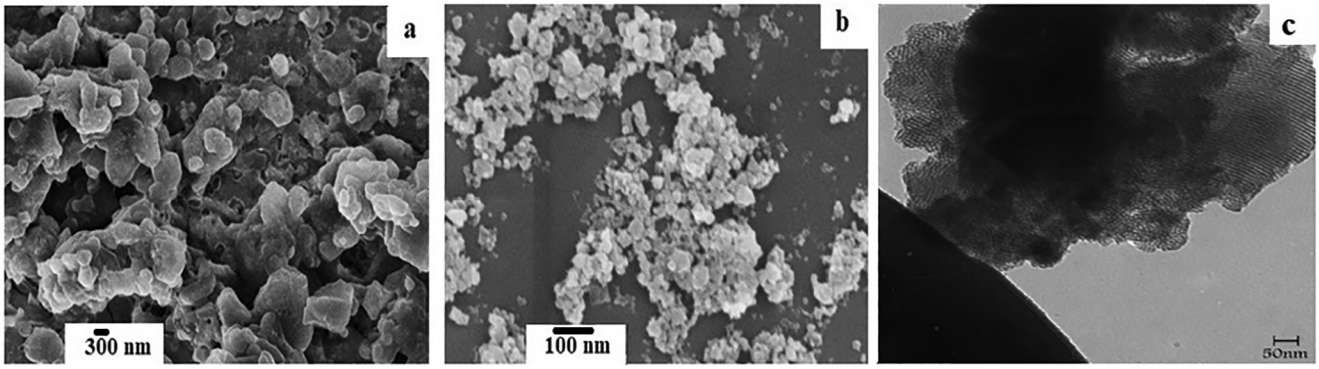

Fig. 4. SEM micrographs of a) ZnO, b) nanoparticle TiO_2 c) TEM micrograph of mesoporous TiO_2.

nanocomposites, RGO-ZnO-(mesoporous TiO_2) and RGO-ZnO-(nanoparticle TiO_2) deposited on an FTO glass substrate. The XRD patterns (Fig. 6) contain sharp peaks from the TiO_2 and ZnO, together with a broad peak at $2\theta = 15–30^{\circ}$ typical of an X-ray amorphous phase, probably arising from a superposition of the RGO and the FTO glass substrate. Fig. 6 also shows no differences in the XRD structures of the nanocomposite containing nanoparticle TiO_2 and mesoporous TiO_2.

3.3. Electrochemical impedance spectroscopy of the layer-structured nanocomposites under UV and visible irradiation

Impedance spectroscopy measurements have been widely used to investigate the charge transfer mechanisms in systems such as the present one [27,28]. The spectra consist of semicircles in the frequency regions. Fig. 7 shows the Nyquist plots derived from electrochemical impedance spectroscopy of the layered nanocomposites RGO- ZnO-(mesoporous TiO_2) and RGO-ZnO-(nanoparticle TiO_2) on FTO substrates under UV and visible light. The Nyquist plots show that both the samples containing nanoparticle TiO_2 and mesoporous TiO_2 showed lower total impedances under UV irradiation than the same samples under visible light. These results may be related to the excitation of the electrons under UV radiation [29].

The band gaps of these samples were determined from the Tauc plots [30] using the relationship proposed by Tauc, Davis, and Mott [31]:

$$(h\nu\alpha)^{1/n} = A(h\nu - Eg) \quad (1)$$

where h is Planck's constant, ν is the frequency of vibration, α is the absorption coefficient, calculated from the equation

$$\alpha = 1/t(\mathrm{Ln}(1/T))$$

where T is the transmittance as shown in Fig. S2(a, b) and t is the thickness of the samples which is considered to be constant and about 1.41(μm) for all samples, according to data in Table (S1), Eg is the band gap, A is a constant and n denotes the nature of the sample transition, and varies from 1/2 to 3. Based on the literature [17], we set m = 1/2 for the present calculations. The bandgap is determined from the point of intersection of the linear portion of the Tauc plot (Fig. 8) with the horizontal axis. This calculation indicated that the band gap in the sample containing nanoparticle TiO_2 is about 3.1 eV, which is smaller than the band gap of the sample containing mesoporous TiO_2 (3.6 eV).Based on the Nyquist plots and band gap information, two mechanisms may be advanced to explain these differences in electrical conductivity, namely differences in the layer thickness between the samples, and the possible formation of nano-sized capacitors on the mesoporous TiO_2**.** These possibilities are discussed below.

Table 2
BET data and mean pore size for mesoporous TiO_2.

Material	Slope	Intercept	S_t (m^2/g)	v_p (cm^3/g)	$\bar{d}$ (nm)
mesoporous TiO_2	0.039	-91×10^{-5}	114.09	0.228	7.9

3.4. Layer thickness of the RGO-ZnO-TiO_2 nanocomposites on FTO glass

The resistance of a given material increases with length, but decreases with increasing cross-sectional area [32]. Thus, one of the parameters which will affect the total impedance is the thickness of the RGO-ZnO-TiO_2 nanocomposites. SEM/EDS analysis across the nanocomposite layer on the FTO glass (Fig. S3) indicates that the deposited layer is uniform cross-section and similar thickness of about 1.43 μm in all the samples (Table S1), with no gap between the nanocomposite layer and the FTO glass. Thus it may be concluded that the total impedance is not affected by variations in the thickness of the deposited layers of the various samples. Furthermore, EDS spot analyses (Fig. S3)

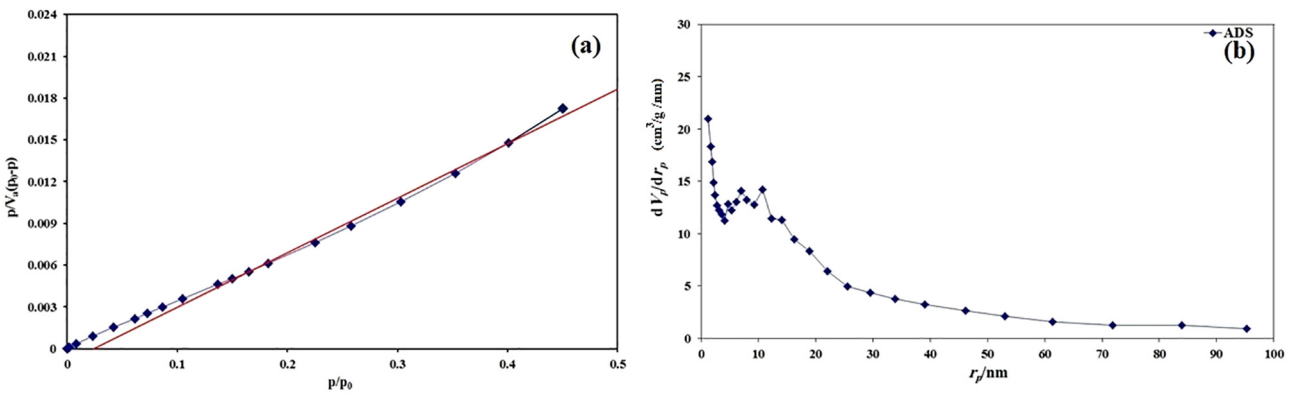

Fig. 5. a) BET plot of mesoporous TiO_2, b) $\frac{dvp}{dr_p}$ vs. r_p (nm) for mesoporous TiO_2.

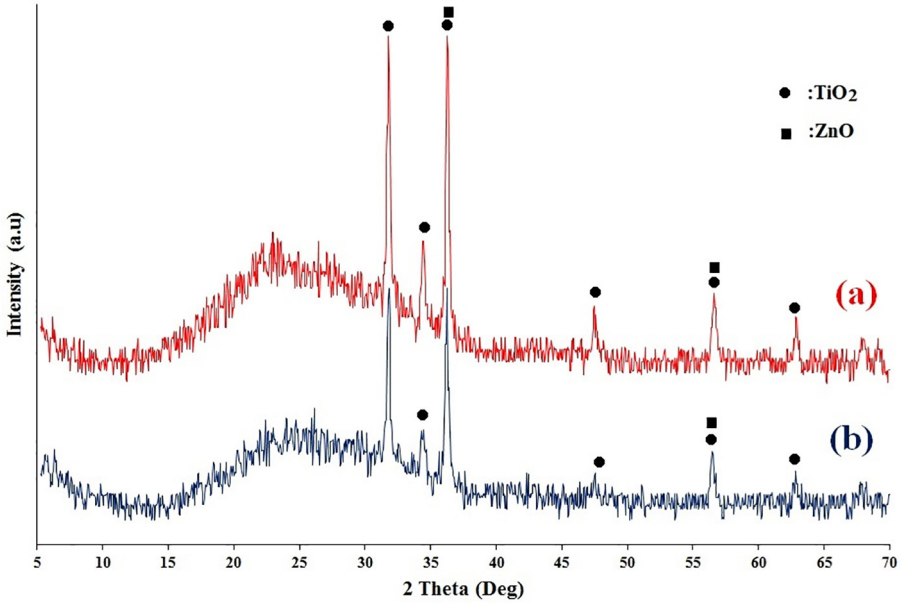

Fig. 6. X-ray diffraction pattern of layered nanocomposites on FTO glass substrates. a) RGO-ZnO-(mesoporous TiO_2), b) RGO-ZnO-(nanoparticle TiO_2).

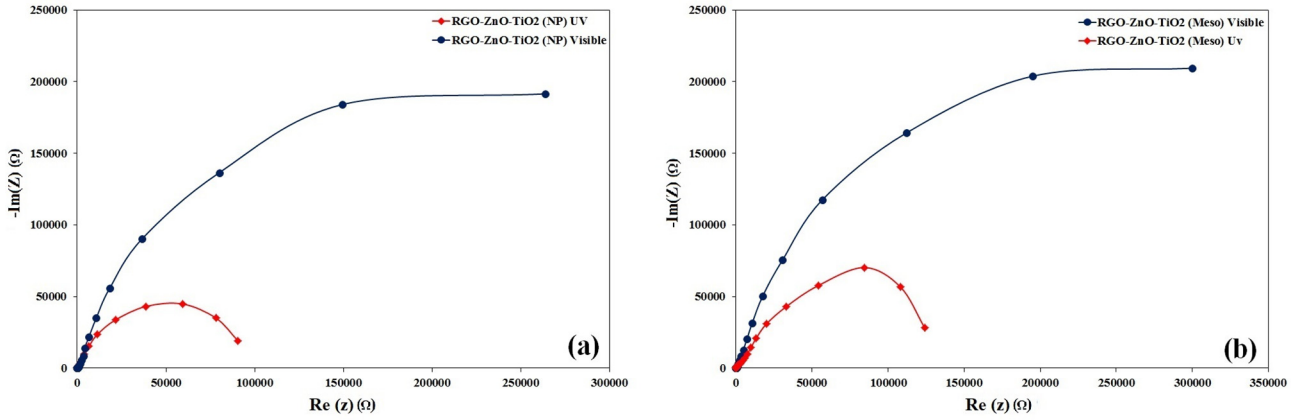

Fig.7. Nyquist plots under UV and visible irradiation, (a) RGO-ZnO-(nanoparticle TiO_2), (b) RGO-ZnO-(mesoporous TiO_2).

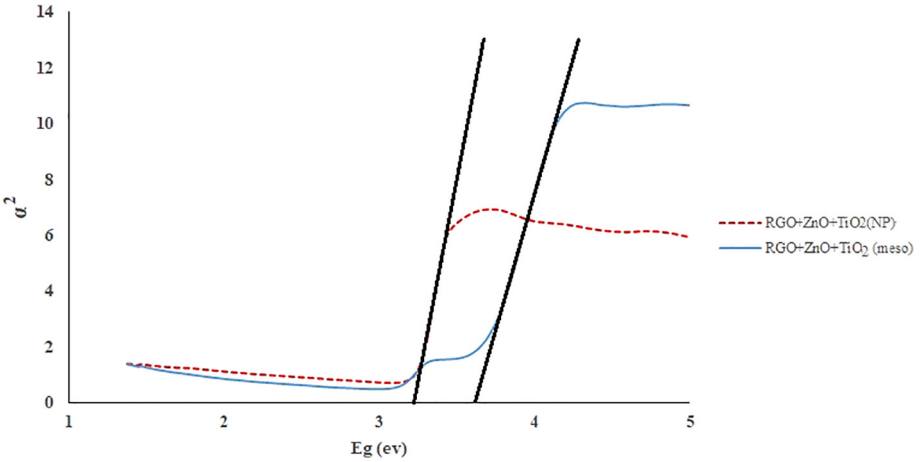

Fig. 8. Tauc plots of RGO-ZnO-(mesoporous TiO_2) and RGO-ZnO-(nanoparticle TiO_2) on FTO glass.

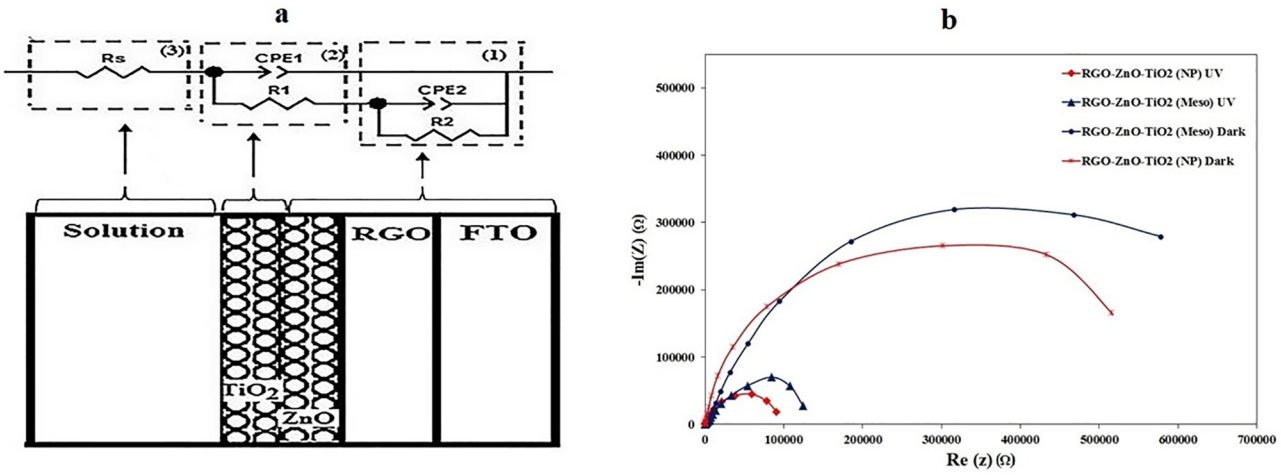

Fig. 9. a) Simulated equivalent circuit for analysis of the electrochemical impedance, b) Nyquist plots in the dark and under UV irradiation of RGO-ZnO-(nanoparticle TiO_2) and RGO-ZnO-(mesoporous TiO_2).

Table 3
Simulated parameters of samples RGO-ZnO-(nanoparticle TiO_2) and RGO-ZnO-(mesoporous TiO_2) under UV and visible irradiation. Sample designations as in Table 1.

Sample	Rs (Ω)	CPE1 (μF)	R1 (Ω)	CPE2 (μF)	R2 (Ω)	Zt (Ω)
1	10.01	14.0	2587	11.1	5.73×10^5	1010
2	10.06	16.9	1330	17.9	1.13×10^5	769
3	11.28	51.9	6918	12.5	6.21×10^5	1271
4	11.86	38.7	1017	12.3	1.56×10^5	1100

taken from points close to the interface (point A) and in the middle of the nanocomposite layer (point B) indicate that the layer components are homogeneous within all the nanocomposite samples.

3.5. Formation of nano-sized capacitors on the mesoporous TiO_2

The spectrum was fitted by an equivalent circuit model composed of two parallel combinations of resistance–capacitance (R-CPE) and one resistance (Rs) in series. Rs is related to I^-/I_3^-, (R1-CPE1) is related to TiO_2 nano layer and (R2-CPE2) corresponding to the FTO-RGO-ZnO layer, and these elements were fitted by Z view software (Fig. 9a) [33,34]. The values of these parameters in Fig. 9a, are collected in Table 3, which suggests that the decreased total impedance (Zt) in the samples under UV irradiation compared with visible irradiation may be related to the decreased charge transfer resistance R2 of the ZnO-RGO-FTO layer. Since this resistance may be related to the RGO-ZnO, layers, this observation could explain the improved efficiency of the reduction of RGO under UV irradiation. To confirm this result, Electrochemical Impedance Spectroscopy (EIS) was carried out under dark condition for the samples (RGO-ZnO-nanoparticle TiO_2) and (RGO-ZnO-mesoporous TiO_2) and the results for these samples under dark conditions were compared to those under UV irradiation (Fig. 9b). The results show that the charge transfer resistance (the radius of the semicircle) in Nyquist diagrams is increased significantly.

Comparison between the parameters of sample 2 (containing nanoparticle TiO_2 under UV) and sample 4 (containing mesoporous TiO_2 under UV) shows that the total impedance is greater in the sample containing mesoporous TiO_2, whereas the interfacial capacitance of the RGO-ZnO layer (CPE2) showed little change but the interfacial capacitance of the TiO_2 (CPE1) decreased from 16.9 μF in the nanoparticle TiO_2 to 38.7 μF in the mesoporous TiO_2. These results could be explained by the formation of nano-sized capacitors within the mesoporous TiO_2 which could be arranged in different ways (in parallel or series) on the surface of the FTO-RGO-ZnO structure, as shown schematically in Fig. 9a. Such a nano capacitor would consist of two conductors separated by a non-conductive region which could be either a vacuum or an electrical insulator such as air as the dielectric. In the present nano capacitor, the conducting electrodes would be formed by the mesoporous TiO_2 under the action of UV light, and the dielectric medium would be the airgap in the pores (Fig. S4).

4. Conclusions

Hybrid semiconductor nanocomposites composed of layers of reduced graphene oxide (RGO), ZnO and both nanoparticle and mesoporous forms of TiO_2 were dip-coated on to FTO glass substrates. The RGO was formed from graphene oxide, reduced under UV radiation at room temperature, then under argon atmosphere at 400 °C for 30 min. and the TiO_2 and ZnO components were synthesized by a sol-gel method. The resulting layered nanocomposites were shown by XRD, DRS-UV, FTIR and FE-SEM techniques to be of homogeneous layer composition and of consistent thickness, with the TiO_2 in the anatase form. Electrochemical impedance spectroscopy (EIS) was used to determine the bandgap and electrical conductivity of the nanocomposites. Analysis of these results showed that when measured under UV irradiation, the nanocomposite containing nanoparticle TiO_2 was more electrically conductive than the nanocomposite containing mesoporous TiO_2. Two possible reasons for this were: (i) differences in the layer thickness of the samples (ruled out by SEM measurements) and (ii) the formation of nano-capacitors on the surface of the ZnO layer. Detailed analyses of the EIS measurements are consistent with this proposed mechanism, in which the pores in the mesoporous TiO_2 act as the dielectric and the conducting electrodes are formed by the action of the UV irradiation on the TiO_2.

Acknowledgements

The authors acknowledge the Islamic Azad University, Najafabad branch, Isfahan, Iran for financial support, and Mr. Chami for technical assistance.

Appendix A. Supplementary data

Supplementary data to this article can be found online at https://doi.org/10.1016/j.mseb.2019.06.003.

References

[1] L. Rimoldi, D. Meroni, E. Falletta, V. Pifferi, L. Falciola, G. Cappelletti, S. Ardizzone,

Photochem. Photobiol. Sci. 16 (2017) 60–66.
[2] C. Han, M.-Q. Yang, B. Weng, Y.-J. Xu, Phys. Chem. Chem. Phys. 16 (2014) 16891–16903.
[3] J. Wang, Y. Li, J. Ge, B.-P. Zhang, W. Wan, Phys. Chem. Chem. Phys. 17 (2015) 18645–18652.
[4] V. Stengl, S. Bakardjieva, T.M. Grygar, J. Bludska, M. Kormunda, Chem. Cent. J. 7 (2013) 41.
[5] T. Xu, L. Zhang, H. Cheng, Catal. B: Environ. 101 (2011) 82–387.
[6] J. Tang, A.J. Cowan, J.R. Durrant, D.R. Klug, J. Phys. Chem. C 115 (2011) 3143–3150.
[7] B. O'Regan, J. Moser, M. Anderson, M. Graetzel, J. Phys. Chem. 94 (1990) 8720–8726.
[8] K. Dai, G. Dawson, S. Yang, Z. Chen, L. Lu, Chem. Eng. 191 (2012) 571–578.
[9] Y. Li, X. Zhou, X. Hu, X. Zhao, P. Fang, J. Phys. Chem. C 113 (2009) 16188–16192.
[10] X. Liu, L. Pan, Q. Zhao, T. Lu, G. Zhu, T. Chen, T. Lu, Z. Sun, C. Sun, Chem. Eng. J. 183 (2012) 238–243.
[11] A.A. Madhavan, A. Mohandas, A. Licciulli, K.P. Sanosh, P. Praveen, R. Jayakumar, S.V. Nair, A.S. Nair, A. Balakrishnan, RSC Adv. (2013) 25312–25316.
[12] X. Liu, L. Pan, T. Lu, Z. Sun, J. Colloid Interface Sci. 394 (2013) 441–444.
[13] F.-T. Johra, W.-G. Jung, RGO–TiO_2–ZnO composites: synthesis, characterization, and application to photocatalysis, Appl. Catal. A 491 (2015) 52–57.
[14] J. Guerrero-Contreras, F. Caballero-Briones, Mater. Chem. Phys. 153 (2015) 209–220.
[15] H. Tian, H. Fan, H. Guo, N. Song, Sensor. Actuat. B 195 (2014) 132–139.
[16] S.S. Kanmani, K. Ramachandran, Renew. Energy 43 (2012) 149–156.
[17] A. Nourbakhsh, S. Abbaspour, M. Masoud, S.N. Mirsatari, A. Vahedi, K.J.D. Mackenzie, Ceram. Int. 42 (2016) (1906) 11901–11911.
[18] R. Garg, N. Dutta, N.R. Choudhury, Rev. Nanomater. 4 (2014) 267–300.
[19] S. Debnath, A. Maity, K. Pillay, J. Environ. Chem. Eng. 2 (2014) 260–272.
[20] L. Tang, Y. Wang, Y. Li, H. Feng, J. Lu, J. Li, Adv. Funct. Mater. 19 (2009) 2782–2789.
[21] Y. Li, Q. Du, T. Liu, X. Peng, J. Wang, J. Sun, Y. Wang, S. Wu, Z. Wang, Y. Xia, L. Xia, Chem. Eng. Res. Des. 91 (2013) 361–368.
[22] P. Sharma, M.R. Das, J. Chem. Eng. Data 58 (2012) 151–158.
[23] Y. Li, J. Ding, J. Chen, C. Xu, B. Wei, J. Liang, D. Wu, Mater. Res. Bull. 37 (2002) 313–318.
[24] T. Lu, L. Pan, H. Li, G. Zhu, T. Lv, X. Liu, Z. Sun, T. Chen, D.H.C. Chua, J. Alloys Cpds. 509 (2011) 5488–5492.
[25] K. Eun-Young, K. Dong-Suk, A. Byung-Tae, Bull. Korean Chem. Soc. 30 (2009) 193–196.
[26] P.I. Ravikovitch, D. Wei, W.T. Chuen, G.L. Haller, A.V. Neimark, J. Phys. Chem. B 101 (1997) 3671–3679.
[27] B. Conings, L. Baeten, H.-G. Boyen, D. Haen, M.K. Van Bael, J.V. Manca, J. Phys. Chem. C 116 (2012) 14237–14242.
[28] R.T. Ginting, C.C. Yap, M. Yahaya, M. Mat Salleh, Appl. Mater. Interfaces 6 (2014) 5308–5318.
[29] S. Pei, H.-M. Cheng, Carbon 50 (2012) 3210–3228.
[30] J. Tauc, Mater. Res. Bull. 3 (1968) 37–46.
[31] X.M. Li, H. Zhu, J. Wei, K. Wang, E. Xu, Z. Li, D. Wu, Appl. Phys. A 97 (2) (2009) 341–344.
[32] M.B. Heaney, Electrical conductivity and resistivity, in: J.G. Webster (Ed.), Electrical Measurement, Signal Processing and Displays, CRC Press, Boca Raton, FL, 2003Ch. 7.
[33] ZView® version 3.4 (2016), Scribner Associates Inc.
[34] R.T. Ginting, C.C. Yap, M. Yahaya, M. Mat Salleh, J. Alloy Compounds 585 (2014) 696–702.